Quantitative Modeling of Superconducting Planar Resonators for Electron Spin Resonance

Stefan Weichselbaumer,[1,2,*] Petio Natzkin,[1,2] Christoph W. Zollitsch,[1,2,†] Mathias Weiler,[1,2]
Rudolf Gross,[1,2,3] and Hans Huebl[1,2,3]

[1]*Walther-Meißner-Institut, Bayerische Akademie der Wissenschaften, 85748 Garching, Germany*
[2]*Physik-Department, Technische Universität München, 85748 Garching, Germany*
[3]*Nanosystems Initiative Munich, 80799 München, Germany*

We present three designs for planar superconducting microwave resonators for electron spin resonance (ESR) experiments. We implement finite-element simulations to calculate the resonance frequency and quality factors as well as the three-dimensional microwave magnetic field distribution of the resonators. One particular resonator design offers an increased homogeneity of the microwave magnetic field while the other two show a better confinement of the mode volume. We extend our model simulations to calculate the collective-coupling rate between a spin ensemble and a microwave resonator in the presence of an inhomogeneous magnetic resonator field. Continuous-wave ESR experiments of phosphorus donors in ^{nat}Si demonstrate the feasibility of our resonators for magnetic resonance experiments. We extract the collective-coupling rate and find good agreement with our simulation results, corroborating our model approach. Finally, we discuss specific application cases for the different resonator designs.

I. INTRODUCTION

Microwave resonators are a key part of any electron spin resonance (ESR) experiment. They enhance the microwave magnetic field at the sample location and offer equally enhanced sensitivity for inductive detection of magnetization dynamics [1,2]. While conventional ESR resonators based on three-dimensional (3D) microwave cavities provide a microwave magnetic field with high homogeneity over a large volume, they suffer from small filling factors and, in turn, a low sensitivity for small samples. Planar microresonators allow the reduction of the mode volume, which, depending on the sample size and geometry, can lead to an increased filling factor and therefore an enhanced sensitivity compared to 3D cavities [3–5]. In addition, planar resonators operated at low temperatures allow superconducting materials to be used, offering small losses and extraordinarily high quality factors. Making use of these advantages has led to a plethora of planar resonator geometries [6–8], applicable in several different fields of expertise. In addition, superconducting resonators have also become key components in the field of circuit quantum electrodynamics (cQED) [9] and have led to a subsequent introduction of cQED concepts in the

field of magnetic resonance [10–13]. The quest for ultrasensitive ESR at low temperatures has led to a range of experiments. Well-known examples are the use of parametric amplification based on superconducting quantum circuits [14,15] or the use of quantum states as a resource to increase the signal-to-noise ratio [16]. Another direction is to increase the coupling rate between a spin ensemble and the microwave resonator to enhance the read-out sensitivity of the measurements. Here, the so-called strong coupling regime has been achieved for several types of spin systems in combination with superconducting resonators [17–21].

Despite inspiring progress in ultrasensitive ESR, so far a quantitative analysis of planar resonator designs and their suitability for achieving strong coupling and enabling straightforward coherent control of spin systems is still missing. Here, we employ finite-element method (FEM) simulations of superconducting planar microwave resonators for calculating the spatial distribution of the microwave magnetic field of three different resonator geometries. This information is crucial in order to judge the performance of the resonator for the specific application. We demonstrate that these simulations can be used not only to predict the resonance frequencies and quality factors but also to allow for a quantitative comparison of the magnetic field homogeneity. Additionally, the simulated magnetic field distribution enables us to calculate the expected collective-coupling rate between the spin

---

*stefan.weichselbaumer@wmi.badw.de
†Present address: London Centre for Nanotechnology, University College London, London WC1H 0AH, United Kingdom.

ensemble and the microwave resonator. Finally, we compare our model predictions to actual continuous-wave ESR data and find good agreement between theory and experiment, including the modeling of power-dependent saturation effects. Here, we show that the modified power saturation confirms the simulations of the microwave magnetic field distribution. In addition, this work compares the various resonator designs with different levels of microwave magnetic field homogeneity. This is relevant in the context of pulsed-ESR experiments, as homogeneous microwave magnetic excitation fields are a key requirement for the coherent control of spin ensembles using rectangular-pulse excitation schemes.

The experimental data presented in this work are recorded at a temperature of 1.5 K, i.e., the resonator is not in its quantum ground state. Chiorescu *et al.* demonstrated, by numerical simulations, that a transition to the classical spin-resonance mechanism occurs when the number of photons in the resonator, n_{ph}, is large compared to the number of spins, N [22]. However, as we will show later, this is not the case for the measurements presented in this paper. Our data therefore allow us to compare the computed effective coupling between the microwave resonator and the spin ensemble at millikelvin temperatures, as the thermal spin polarization can be taken into account [21].

The paper is organized as follows. First, we introduce three different planar resonator designs and present fundamental design considerations. We then introduce the concept of spin-photon coupling in the context of electron spin resonance and show how the collective-coupling rate can be computed in the presence of an inhomogeneous microwave magnetic field. Subsequently, we present our simulation approach. We quantitatively analyze the field homogeneity of two of the resonator designs and show that one particular design offers an increased field homogeneity compared to the other designs. In the following experimental section, we first confirm the feasibility of our simulation approach. The second part of the experimental section is dedicated to continuous-wave ESR experiments on an ensemble of phosphorus donors in silicon (Si:P). We extract the collective-coupling rate and find good agreement between the theoretical model and the experimental data. Finally, we also model the power-dependent saturation of the collective-coupling rate.

II. THEORETICAL CONSIDERATIONS

A. Microwave resonator designs

In the following, we present the sample layout and the resonator designs presented in this paper. Figure 1(a) displays the generic design of a chip featuring a central feed line, designed in coplanar waveguide (CPW) geometry [23], with two connection pads at the edges of the substrate. More details and characteristic parameters are given in Sec. III A.
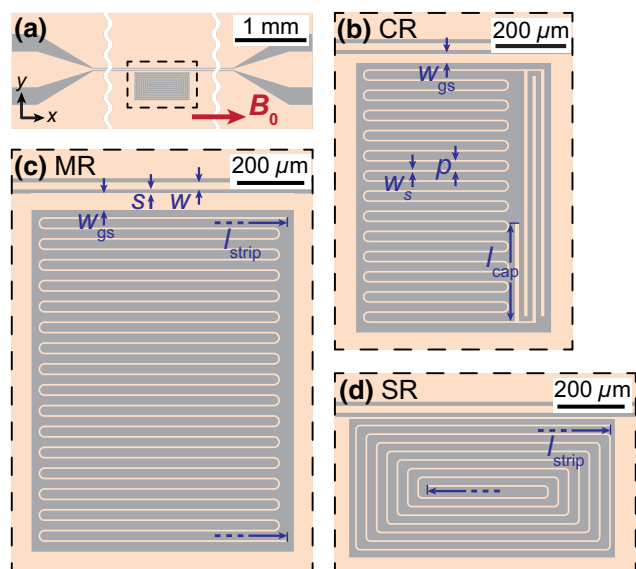

FIG. 1. A schematic illustration of the resonator designs studied in this work. For details and parameters, see the text. (a) The generic device layout. A central feed line with two connection pads excites the resonators, which are placed in the proximity of the feed line (dashed box). (b) The capacitively shunted meander resonator (CR) consisting of a interdigitated finger capacitor shunting a meandering inductor. (c) The meander resonator (MR) is a half-wavelength resonator consisting of a long meander-shaped strip. (d) For the spiral resonator (SR), the meander-shaped strip is arranged in a two-dimensional (2D) coil-like structure, providing an increased field homogeneity.

The planar microwave resonator structure is placed in the proximity of a microwave feed line (dashed box). Figures 1(b)–1(d) show the three discussed resonator designs, which are (b) a CR, (c) an MR, and (d) an SR. For the MR, the capacitance is provided by the intraline capacitance, with a higher inductance-to-capacitance ratio than the CR. The SR design also relies on the intraline capacitance but provides a more homogeneous magnetic field distribution than the MR design.

The CR is a so-called lumped-element microwave resonator [24–26], where the capacitance and the inductance are most obviously visible in the form of the interdigital capacitor and the meandering inductor. Nevertheless, a numerical analysis of the resonance frequency as a function of the interdigital capacitance finger length [see Fig. 4(a)] suggests that there is a finite capacitance contained in the meandering structure for the design displayed. In consequence, the meandering resonator is the logical next step, where the interdigital capacitor is completely missing. The explicit missing capacitance is compensated by an enhanced total length of the resonator structure. An alternative viewpoint is to think of the meander resonator as a waveguide structure, where the length of the conductor supports a standing-wave pattern of the microwave [27]. Here, the length of the meander-shaped strip of the MR and

SR corresponds to half of the wavelength of the resonance frequency and thus supports this picture.

The meander shape of the CR and MR results in a counter flow of the high-frequency currents in neighboring meandering strips. This enables a localization of the electromagnetic field close to the surface. In addition, this also leads to a significant inhomogeneity of the microwave magnetic field B_1 in close proximity to the structure. Moreover, a fast decay of the microwave excitation B_1 field in the z direction, i.e., out of the plane of the microwave resonator [see Figs. 2(a) and 2(c)] is obtained. The characteristic decay length of the B_1 field in the z direction is related to the distance between adjacent wires, which is 20 μm in our design. Although this can be beneficial for the measurement of ultrathin spin samples, for most pulsed-ESR experiments, using rectangular-pulse excitation schemes, the large field inhomogeneity is undesirable and elaborate techniques have been proposed to compensate the B_1 inhomogeneity [28–32]. A suitable resonator design leading to a significant reduction of the magnetic field inhomogeneity comes in the form of a spiral resonator geometry as displayed in Fig. 1(d). Here, neighboring lines have a parallel flow of current, resulting in a much better homogeneity of the B_1 field as shown in Figs. 2(b) and 2(d). Note that the field now extends significantly further in the z direction and the characteristic decay length is of the same order of magnitude as the lateral dimensions of the whole resonator.

The design resonance frequency f_r of the superconducting microwave resonators discussed here is set to a value around 5 GHz. This optimizes the surface impedance and/or losses of the structure (which increase with increasing frequency [33]), while keeping a reasonably high frequency. Additionally, our experimental setup is designed to operate in the frequency band of 4–8 GHz. In general, the resonance frequency of a LC oscillator is given by $f_r = 1/(2\pi\sqrt{LC})$, with an effective inductance L and capacitance C. Changing the length of the capacitor finger l_{cap} for the CR or the total inductor length l_{strip} for the MR and SR allows us to tune the resonance frequency to the desired value.

A further key parameter of a microwave resonator is the quality factor Q, which is given by $Q = f_r/(2\kappa/2\pi)$, where $\kappa/2\pi$ is the loss rate of the resonator [measured as the half width at half maximum (HWHM) of the resonance line]. One can distinguish between internal and external losses with corresponding quality factors given by the following:

$$\frac{1}{Q} = \frac{1}{Q_{ext}} + \frac{1}{Q_{int}}. \qquad (1)$$

The quality factors are linked to the external and internal loss rates according to $Q_{ext} = f_r/(2\kappa_{ext}/2\pi)$ and $Q_{int} = f_r/(2\kappa_{int}/2\pi)$. The internal losses, including radiation, resistive, and dielectric losses [34], are typically very small
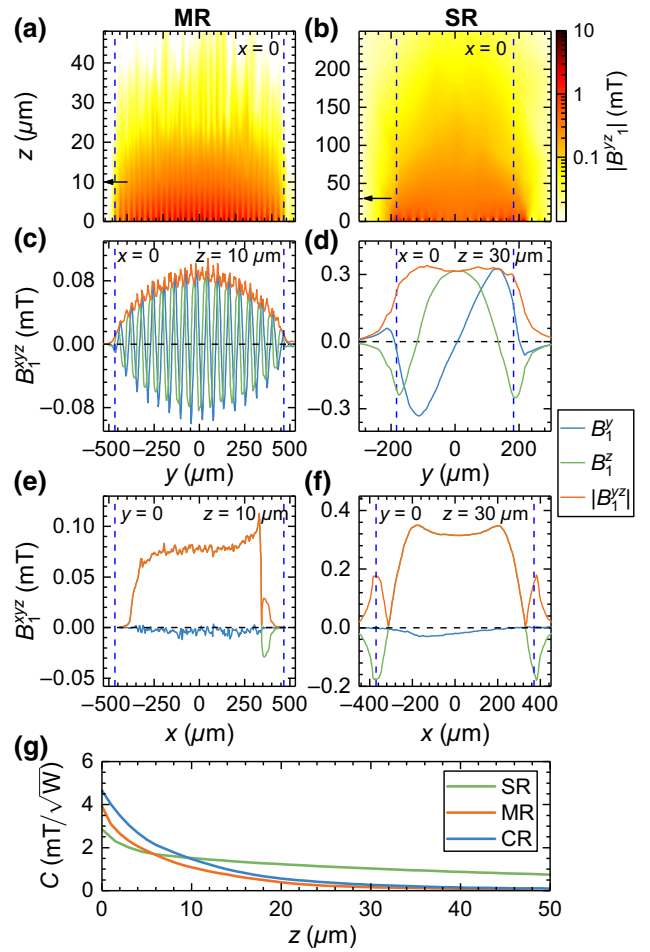

FIG. 2. The simulated magnetic field distribution $|B_1^{yz}|$ for the (a) MR and (b) SR in the y-z plane. Antiparallel current flow in adjacent wires results in a highly inhomogeneous field for the MR, while parallel current flow leads to a more homogeneous field for the SR. The magnetic field components B_1^y and B_1^z as well as the magnitude $|B_1^{yz}|$ at fixed distance [arrows in panels (a) and (b)] are plotted for the (c) MR and (d) SR along the y axis and for the (e) MR and (f) SR along the x axis. (g) The conversion factor C of the different resonators as a function of the distance z above the resonator for two different sample geometries (see text). The MR and CR show larger maximum values but decrease faster with increasing distance compared to the SR.

in superconducting resonators and internal quality factors above 10^7 have been reported [35]. The external loss rate κ_{ext} describes the coupling to the "environment," which in this instance is the feed line. Technically, this coupling can be either of a mainly capacitive or inductive nature, depending on whether the contact point of the resonator is close to an antinode of the electric or magnetic field. It can be controlled by the separation between the resonator and the feed line. Table I summarizes the geometric parameters as well as the resonance frequency and quality factors of the resonators presented in this work.

TABLE I.   The parameters for the three resonator geometries, extracted at $T = 1.5$ K. The resonance frequency as well as the quality factors are extracted with a Si:P crystal mounted on the resonator and at a finite magnetic field. The applied sample power is $P_S = -110$ dBm for the CR and $P_S = -115$ dBm for the SR and/or MR.

Resonator	Dimensions (μm^2)	V_m (μm^3)	f_r (GHz)	Q	Q_{ext}	Q_{int}	$g_{eff,exp}$ (kHz)	$g_{eff,theo}$ (kHz)	d_{gap} (μm)
SR	770×410	1.88×10^7	3.7598	12 930	31 434	21 968	438 ± 32	511.2	2.53 ± 0.82
MR	760×1000	1.52×10^7	4.3305	1688	2155	7791	461 ± 32	627.6	2.23 ± 0.19
CR	580×800	1.41×10^7	4.5398	31 262	89 694	47 987	384 ± 8.4	658.0	3.79 ± 0.09

B. Spin-photon coupling in electron spin resonance

We now turn to the effective coupling between the spin ensemble and the microwave magnetic field mode provided by the resonator. The vacuum coupling strength g_0 between a single spin and the electromagnetic modes of a microwave resonator is given by the following [10]:

$$g_0 = g_s \mu_B B_{1,0}/2\hbar, \qquad (2)$$

where g_s is the electron g factor of the spin ensemble, μ_B is the Bohr magneton, and $B_{1,0}$ describes the zero-point or vacuum fluctuations of the magnetic field inside the resonator. Assuming a homogeneous microwave-field distribution, $B_{1,0}$ can be expressed as [36] $B_{1,0} = \sqrt{\mu_0 \hbar \omega_r/(2V_m)}$, where μ_0 is the vacuum permeability, $\hbar$ is the reduced Planck constant, and V_m is the mode volume of the resonator. Applying this to a typical coplanar waveguide resonator with a signal line width in the order of 10 μm and a resonance frequency in the order of 3 GHz, g_0 can be roughly estimated to 10 Hz [36–38]. Nevertheless, and as discussed below, lumped-element resonators typically have a complex spatially dependent microwave-field distribution, which has to be taken into account. An increase in the coupling increases the sensitivity of the ESR measurements and ultimately allows for a high degree of cooperativity or even strong coupling [39]. When considering not only a single spin but a spin ensemble with N noninteracting spins, the interaction between the whole spin ensemble and the resonator can be improved by making use of collective-coupling effects [40], which predict an enhancement by a factor of $\sqrt{N}$, leading to an effective coupling strength $g_{eff} = g_0\sqrt{N}$. The collective-coupling strength for a homogeneous $B_{1,0}$ distribution can then be written as follows [41]:

$$g_{eff,hom} = \frac{g_s \mu_B}{2\hbar} \sqrt{\frac{1}{2}\mu_0 \hbar \omega_r \rho_{eff} \nu}. \qquad (3)$$

Here, we have substituted the number of spins N by $N = \rho_{eff}V = \rho P(T)V$, where ρ is the spin density, $P(T)$ is the thermal polarization of the spin ensemble's transition, and V is the volume of the spin sample [21]. The filling factor $\nu = V/V_m$ defines the ratio of the Si:P crystal volume to the mode volume of the resonator. This is a crucial parameter

in ESR experiments, as the detected ESR signal is directly proportional to the filling factor [1].

We note again that Eq. (3) assumes a homogeneous distribution of the B_1 field over the Si:P crystal. Moreover, the equation does not consider the orientation of the static magnetic field B_0 relative to the B_1 field required for exciting ESR transitions, i.e., $B_0 \perp B_1$ [1].

As shown in the Appendix, the inhomogeneity can be accounted for by integrating the microwave magnetic field over the Si:P crystal and the cavity volume, respectively, resulting in the following:

$$\nu = \frac{\int_{sample} |B_1(\vec{r})|^2 \, dV}{\int_{cavity} |B_1(\vec{r})|^2 \, dV}. \qquad (4)$$

In our FEM simulations, we compute the B_1 spatial distribution and export it in discrete volume elements ΔV. Thus, rewriting Eq. (4) in the form of a Riemann sum allows us to numerically compute the filling factor and hence the effective coupling. In detail, we derive an expression that accounts for both the inhomogeneity of the microwave magnetic field and the excitation condition (for ESR excitation, $\vec{B}_1$ and $\vec{B}_0$ are chosen to be perpendicular to each other):

$$g_{eff,inhom} = \frac{g_s \mu_B}{2\hbar} \sqrt{\frac{1}{2}\mu_0 \hbar \omega_r \rho_{eff} R_{yz}}. \qquad (5)$$

This expression is equivalent to Eq. (3), replacing the filling factor ν by the term

$$R_{yz} = \frac{\sum_V |B_{1,sim}^{yz}(\vec{r})|^2}{\sum_{V_m} |B_{1,sim}^{xyz}(\vec{r})|^2}. \qquad (6)$$

Here, the sum in the numerator accounts for all numerically computed microwave magnetic field amplitudes in the Si:P crystal volume V that fulfill the excitation condition required for exciting an ESR transition. For our chosen geometry, this is the field amplitude in the y-z plane $\left|B_1^{yz}\right| = \sqrt{(B_1^y)^2 + (B_1^z)^2}$. The denominator can be understood as a normalization factor and thus accounts for the total magnetic field amplitude B_1^{xyz} in the mode volume V_m. Both sums take the field amplitudes B_1^{yz} and B_1^{xyz} at

all available volume elements ΔV computed by the FEM simulations (see Sec. III A) into account. Here, we only consider the half-space above the substrate to be filled with the spin ensemble; thus R_{yz} is naturally limited to $\nu = 0.5$. For realistic resonator structures, this value is further reduced when components of the B_1 field are aligned parallel to the static magnetic field and thus do not contribute to an ESR excitation.

Equations (5) and (6) allow us to calculate and theoretically predict the achievable collective-coupling strength of a spin ensemble coupled to an arbitrary microwave resonator geometry, as long as the magnetic field distribution is known. Note that Eq. (5) in combination with (6) also includes effects originating from thermal polarization, as $\rho_{\mathrm{eff}} = \rho P(T)$. In the following, we will calculate g_{eff} using the magnetic field distribution obtained for our resonator geometries using the FEM simulations, present experimental data for those resonators, and thereby corroborate our theoretical model.

III. FINITE-ELEMENT SIMULATIONS

A. Simulation setup

For our FEM simulations, we use the commercial microwave simulation software package CST MICROWAVE STUDIO 2016 [42]. Technically, our modeling takes the entire chip into account. We start with the definition of the substrate material (here, silicon) with the dimensions of 6 mm × 10 mm × 0.525 mm. On top of the substrate, we model the superconducting film, using a 150-nm-thick perfect electrical conductor for simplicity. Note that we do not take the kinetic inductance [33,43] or the finite penetration depth into account. Figure 1(a) displays the generic design of the feed line. The width of the signal line is $w = 20~\mu$m and the distance between the signal line and the ground plane is $s = 12~\mu$m, corresponding to an impedance of 50 Ω [44]. The wire thickness of the resonator itself is $w_s = 5~\mu$m with a spacing of $p = 20~\mu$m. For the SR, the spacing is $p_x = 30~\mu$m in the x direction and $p_y = 20~\mu$m in the y direction.

In our experiments, a spin ensemble hosted in a silicon crystal interacts with the microwave magnetic field of the resonator. To take the finite dielectric constant of silicon into account and to model the properties of the microwave resonator accurately, we position a box-shaped silicon body with dimensions of 3.4 mm × 3.4 mm × 0.42 mm on top of the resonator. In our simulations, we apply the microwave signal to the structure via one of two waveguide ports that are defined at both ends of the microwave feed line. The power applied to the feed line in our simulations is $P = 0.5$ W. In our simulations, we consider only the linear response regime, i.e., any nonlinear response is not accounted for. The complete model is fully parameterized, allowing us to efficiently explore the influence of a wide range of parameters on the resonator parameters.

The 3D model is divided into tetrahedral mesh cells with a minimum edge length of 0.15 μm. During the simulation, the mesh is adapted automatically to increase the quality of the mesh [42]. Decreasing the mesh size further does not lead to a change of the obtained results; therefore, we conclude that our simulations converge. The microwave magnetic field distribution is exported in a discretized lattice with a pixel size of $1 \times 1 \times 1~\mu$m^3 for the MR and/or CR and $1.5 \times 1.5 \times 1.5~\mu$m^3 for the SR, respectively.

B. Magnetic field amplitude rescaling

In this section, we explain how we adjust the experimental and simulated microwave magnetic field amplitude. We match the field amplitude obtained by the simulations B_1^{sim} to the experimental conditions by rescaling B_1^{sim} to obtain the same photon number in simulation and experiment. The average photon number in a resonator is given by the following:

$$n_{\mathrm{ph}} = \frac{\kappa_{\mathrm{ext}}}{\kappa^2} \frac{P_S}{\hbar \omega_r}, \qquad (7)$$

where P is the applied microwave power. We calculate a rescaling factor $n_{\mathrm{exp}}/n_{\mathrm{sim}}$ with the average number of photons in the resonator for the experiment, n_{exp}, and the simulation, n_{sim}. For the calculations presented below, we rescale the microwave magnetic field amplitude according to the following:

$$B_1 = B_1^{\mathrm{sim}} \sqrt{n_{\mathrm{exp}}/n_{\mathrm{sim}}}. \qquad (8)$$

C. B_1 magnetic field homogeneity

In this section, we present FEM simulations of the microwave magnetic field distribution of the different resonator geometries and analyze the field homogeneity with respect to a finite Si:P crystal size. For the comparison of the field amplitude and homogeneity between the MR and SR, we rescale the magnetic field amplitude for both resonators to an average photon number of 10^{12} photons, which corresponds to an input power of approximately -19 dBm for the SR (-14.5 dBm for the MR). This allows us to quantitatively compare both designs, independent of their respective quality factors.

To visualize the field homogeneity, we show the absolute magnetic field $|B_1^{yz}|$ in the y-z plane ($x = 0$) for the MR and SR in Figs. 2(a) and 2(b), respectively. The vertical dashed lines mark the lateral extent of the resonator. The origin in the x-y plane is chosen to be the center of the resonator.

In the MR, the microwave current in adjacent wires flows antiparallel, resulting in opposing microwave magnetic fields. This is reflected in the homogeneity plot in

panel (a) and is also the reason for the fast decay of the magnetic field in the far field. In contrast, the coil-like arrangement of the inductor wire in the SR leads to a parallel current flow in the two halves of the resonator and therefore to a larger homogeneity. Furthermore, the magnetic field generated by neighboring strips does not cancel in the far field and decays slower than for the MR (note the different scaling of the ordinate). To further highlight the difference between the two designs, we show cuts at a fixed distance above the resonator [arrows in panels (a) and (b)] for $x = 0$ and plot the components B_1^y and B_1^z as well as the magnitude $|B_1^{yz}|$ for the MR and SR along the y axis in Figs. 2(c) and 2(d), respectively. The oscillatory behavior of the magnetic field can be clearly seen for the MR, while homogeneous excitation is obtained for the SR. In Figs. 2(e) and 2(f), we plot the field components at a fixed distance z above the resonator along the x axis. Along this axis, the field homogeneity of the MR is significantly improved.

The MR generates a maximum field of $|B_1^{yz}| = 0.1$ mT at a distance of $z = 10$ μm, compared to 0.35 mT at $z = 30$ μm for the SR. For a more detailed analysis, we evaluate the conversion factor C, which is defined as follows [1]:

$$C = \frac{|B_{1,\mathrm{mean}}^{yz}(z)|}{\sqrt{QP_S}}, \qquad (9)$$

where Q is the resonator quality factor and P_S is the applied microwave power. We assume a sample with xy dimensions much larger than the lateral extent of the resonator. $B_{1,\mathrm{mean}}^{yz}(z)$ is the mean microwave magnetic field in a slice with a thickness of 1 μm (1.5 μm for the SR), with dimensions corresponding to the exported field distribution. The conversion factors for the three resonators are displayed in Fig. 2(e) as a function of the distance z above the resonator. Directly above the resonator, the MR and CR show the highest conversion factors, with values up to 4.6 mT/$\sqrt{\mathrm{W}}$. This value is more than 1 order of magnitude larger than that of commercially available resonators. When the distance to the resonator increases, the conversion factors of the MR and CR decreases faster than for the SR. This is due to the large B_1 inhomogeneity and the fast decay along the z direction of the MR and CR. Please note that due to the different quality factors of the resonators, the conversion factors do not allow a direct comparison of the obtained maximum B_1 amplitude.

The simulated 3D field distribution can also be used to estimate the mode volume V_m, as the region, where the field amplitude decays to 1% of its maximum value. As can be seen in Table I, the mode volume of the SR is increased compared to the other designs, particularly in regard to the smaller lateral dimensions.

IV. EXPERIMENTAL DETAILS

A. Sample fabrication and measurement setup

To fabricate the sample, we first sputter deposit a 150-nm thin layer of Nb with a 10-nm Al capping layer on a high resistivity (>3 kΩ) $^{\mathrm{nat}}$Si substrate with a thickness of 525 μm (we do not take the Al capping layer into account in our simulations). The Al capping layer is introduced to prevent oxidation of the Nb layer. The resonators are patterned using a standard electron-beam lithography process and subsequently etched using chemical wet etching for the Al as well as reactive-ion etching for the Nb layer. The sample chip is then placed into a copper sample holder and connected to two microwave SubMiniature A end-launch connectors. The sample holder is mounted into a helium gas-flow cryostat operated at $T \approx 1.5$ K for all of our experiments.

Figure 3(a) schematically depicts the microwave circuitry of our experiments. For the ESR experiments, we apply an external magnetic field parallel to the Nb film plane provided by a superconducting solenoid. We measure the complex microwave transmission amplitude S_{21} by connecting the sample to the two ports of a vector-network analyzer (VNA). Thereby, we can determine the
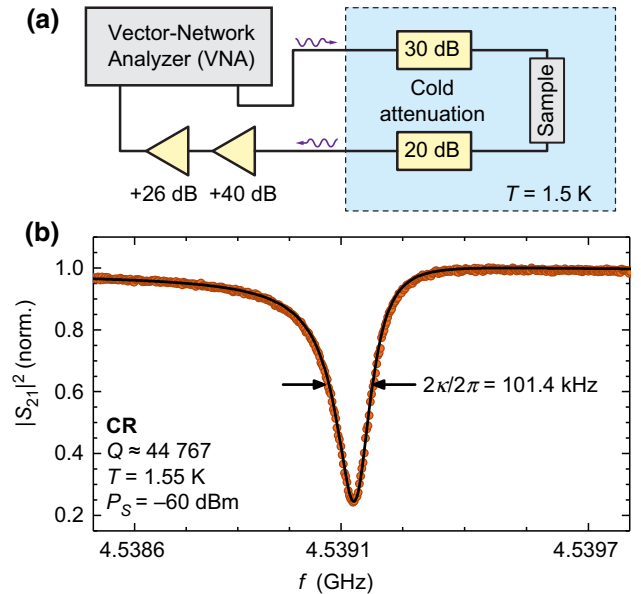

FIG. 3. (a) A schematic of the experimental setup. The sample holder is mounted inside a cryostat with a temperature $T \approx 1.5$ K. Transmission through the sample is measured by a VNA. The signal is attenuated inside the cryostat to suppress room-temperature thermal-microwave photons and is subsequently amplified at room temperature before detection. (b) An exemplary transmission $|S_{21}|^2$ as a function of the frequency (data points), recorded at zero magnetic field without a mounted Si:P crystal. A fitting routine (solid line) allows us to extract the resonance frequency, line width, and external coupling rate from the transmission dip.

uncalibrated power transmission $|S_{21}|^2$ of the sample. The signal is attenuated by 30 dB (20 dB) in the input (output) line inside the cryostat to avoid saturation of the ESR transitions by room-temperature thermal-microwave photons. The signal is amplified by two room-temperature low-noise amplifiers before detection.

Figure 3(b) shows an exemplary measurement, where the transmission $|S_{21}|^2$ (points) is plotted against the frequency. The measurement is recorded at zero magnetic field and no sample is mounted on the chip. The attenuators are not present. For the normalization, we set the off-resonant transmission to one. When the excitation frequency is in resonance with the microwave resonator, the transmission drops to about 0.15. In order to extract the resonance frequency and the line width, as well as the coupling rate of the microwave resonator to the microwave feed line from the measured complex S_{21} data, we use a robust circle fit (solid line) described by Probst *et al.* [45].

We summarize the relevant parameters for the resonators used in this work in Table I. The resonance frequency as well as the quality factors are extracted from transmission measurements with a mounted Si:P crystal, as described above. The extraction of the collective-coupling rate, its theoretical calculation, and the estimation of the Si:P crystal-resonator gap d_{gap} are described in Sec. IV D.

B. Comparison of the resonator parameters: Experiments versus the FEM simulations

To verify our simulation approach, we fabricate two sample chips with several capacitively shunted resonators (CR). We measure the complex transmission S_{21} with no external applied magnetic field and extract the resonance frequency as well as the external coupling rate. The measurements are performed without a sample; therefore, we exclude the additional silicon body on top of the resonator in the simulations for this section.

In Fig. 4(a), we compare the measured and simulated resonance frequency as a function of the length of the capacitor finger l_{cap}. An increase in l_{cap} results in a higher total capacitance and therefore a decrease in the resonance frequency. The simulations (orange line) reproduce the measurement results quantitatively to within 1.6% of the resonance frequency. Nevertheless, the frequency is slightly overestimated, which we attribute to modeling the superconductor as a perfect electric conductor, thereby neglecting the effects of superconducting properties. In panel (b), the external coupling rate κ_{ext} is plotted as a function of the width of the ground line w_{gs}, separating the resonator window from the CPW [see Fig. 1(b)]. As expected, reducing w_{gs} increases the coupling. The coupling rate roughly shows an exponential behavior with the separation between the resonator and the feed line. This is due to the screening of the microwave radiation of the
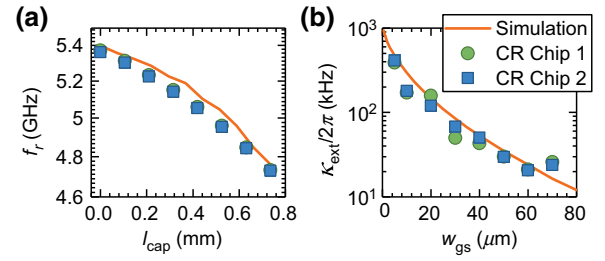

FIG. 4. A comparison of two chips containing several CRs with finite-element simulations. Filled squares and circles represent experimental data. The solid orange lines are obtained from the FEM simulations. (a) Tuning of the resonance frequency by adjusting the length l_{cap} of one of the fingers of the capacitor. The resonance frequency drops with increasing length l_{cap}. (b) Tuning of the external coupling κ_{ext} between the resonator and the feed line by changing the width w_{gs} of the small metal strip, separating the resonator from the signal line.

feed line by a metallized strip with a width w_{gs} between the two circuit elements. Again, we find excellent qualitative agreement between the experimental data and the FEM simulations.

C. Continuous-wave electron spin resonance

We perform continuous-wave ESR measurements by placing a phosphorus-doped ^{nat}Si sample with a donor density of $\rho = 2 \times 10^{17}$ cm^{-3} in flip-chip geometry on the sample chip. For the following measurements, both attenuators in the cold part of the microwave circuitry are in place.

In Fig. 5(a), we show the normalized transmission $|S_{21}|^2$ as a function of the probe frequency and the static applied magnetic field B_0 relative to the center resonance field B_{res}. The transmission is reduced to about 0.35 when the excitation frequency is in resonance with the microwave transmission. We further observe a shift of the resonance frequency over the displayed magnetic field range, which we attribute to the magnetic field dependent kinetic inductance of the superconductor. The applied magnetic field leads to an increase in the kinetic inductance and thereby also the total inductance of the resonator, changing f_r. Further, we observe two distinct features at ± 1.7 mT, which are identified as the two hyperfine transitions of the phosphorus donors in silicon. For a more detailed analysis, we determine the resonator line width κ as a function of the applied magnetic field. For this, we extract κ from the transmission spectra for each magnetic field step. This corresponds to a continuous-wave ESR measurement, where the quality factor (absorption signal) of the resonator is measured [1]. We plot κ as a function of the applied static field in Fig. 5(b). In this representation, the two peaks correspond analogously to the two hyperfine transitions. In the magnetic field range between the two peaks, we observe additional broad features corresponding to two additional
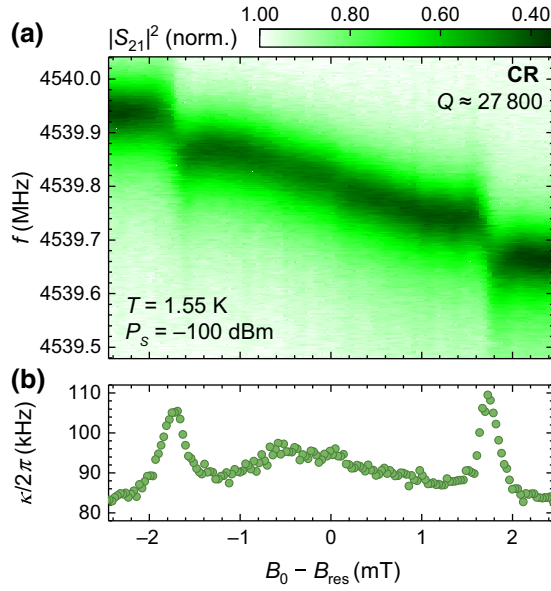
FIG. 5.   (a) The transmission $|S_{21}|^2$ as a function of the frequency and the applied magnetic field. The frequency-dependent absorption dip corresponds to the resonator, while the two distinct features indicate the phosphorus hyperfine transitions. (b) The extracted line width $\kappa/2\pi$ (HWHM) as a function of the magnetic field. The two peaks correspond to the hyperfine transitions. The features at intermediate fields are compatible with Pb_0/Pb_1 dangling bond defects and P_2 dimers (see text for details).

FIG. 6.   (a) The measured line width $\kappa/2\pi$ of the spiral resonator for the high-field hyperfine transitions of phosphorus donors in ^{nat}Si. The solid line is a fit to Eq. (10) to extract g_{eff}, κ_c and γ_s (see text). (b) The dependence of the filling factor R_{yz} on a finite gap d_{gap} between the resonator and the Si:P crystal. A reduction of R_{yz} from the ideal value (dashed line) is due to magnetic field components parallel to the static magnetic field. The CR and MR show a more significant decrease compared to the SR due to the short decay length of the dynamic magnetic field.

onset of saturation effects at microwave powers as low as -120 dBm.

D. Analysis of the collective coupling

In the following, we analyze the collective coupling between the microwave resonator and the high-field hyperfine transition of the phosphorus donors. In Fig. 6(a), we show the extracted line width plotted against the applied static field, relative to the resonance field of the high-field hyperfine transition. The microwave power applied to the sample is $P_S = -110$ dBm to avoid saturation of the ESR transition.

The line width κ in the weak coupling regime can then be described as follows [50]:

$$\kappa = \kappa_c + \frac{g_{eff}^2 \gamma_s}{\Delta^2 + \gamma_s^2}, \qquad (10)$$

where κ_c is the off-resonant line width of the resonator, γ_s is the spin line width (full width at half maximum), and g_{eff} is the collective-coupling rate. The detuning Δ is defined as $\Delta = g_s \mu_B (B_0 - B_{HF})/h$. We fit Eq. (10) in combination with a linear background (dashed line) to the data presented in Fig. 6(a) (solid lines). We extract a collective-rate $g_{eff}/2\pi = 438 \pm 32$ kHz. The resonator line width at $B_0 - B_{HF} = 0.49$ mT is $\kappa/2\pi = 72.4 \pm 0.5$ kHz. The inhomogeneously broadened spin line width (half width at half maximum) is $\gamma_s/2\pi = 3.67 \pm 0.13$ MHz, corresponding to a line width $\delta B = 131.1 \pm 4.6$ μT.

spin systems. The resonance fields of those peaks are compatible with (i) dangling bond defects at the Si/SiO$_2$ interface, known as Pb_0/Pb_1 defects [46,47] (at approximately -0.5 mT), and (ii) exchange-coupled donor pairs forming P_2 dimers [48,49] (at approximately 0 mT).

Note that we do not perform a field calibration to absolute values. The static magnetic field in our experiments is generated by a large superconducting solenoid, which exhibits a significant amount of trapped flux. This leads to field offsets in the order of approximately 10 mT. However, in our work the absolute magnetic field applied to the Si:P crystal is only of subordinate interest and we therefore plot the magnetic field relative to the expected center resonance field.

For the applied power of $P_S = -100$ dBm, corresponding to an average photon number of $n \approx 7.8 \times 10^4$ [cf. Eq. (7)], we observe the onset of saturation effects (see Sec. IV E). In order to calculate the collective coupling between the spin ensemble and the microwave resonator in the next section, we choose a data set in which the microwave power is decreased to -110 dBm (2.5×10^3 photons on average). We also point out the importance of the additional attenuators in the setup to suppress thermal-microwave-noise photons generated at room temperature. Without the attenuation, we already observe the
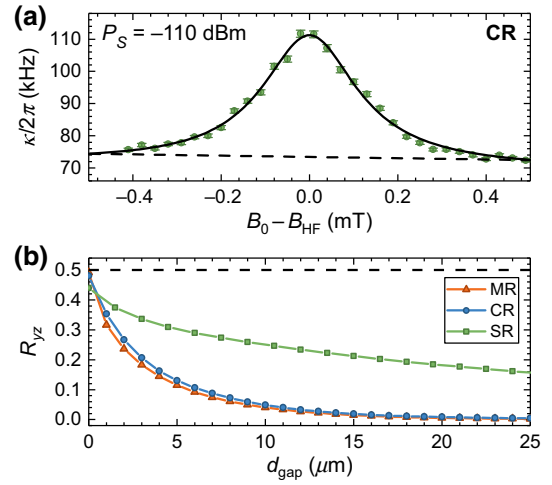
This is in agreement with literature values for ^{nat}Si with a natural abundance of 4.7% ^{29}Si nuclei [51,52]. Note that the line shape of the ESR transition depends on the residual ^{29}Si concentration in the sample [51]. For small ^{29}Si concentrations, the line shape is given by a Lorentzian. However, the transition from a Lorentzian to a Gaussian line shape happens at a ^{29}Si concentration of approximately 5%, which is the case for our sample. For our analysis, we therefore perform fits with Gaussian and Lorentzian line shapes. We only observe good agreement when fitting a Lorentzian peak, confirming that the use of Eq. (10) is valid.

For a first theoretical estimate of g_{eff}, we assume an effective spin density $\rho_{eff} = 0.5\rho$, as only half of the spins contribute to each hyperfine transition [53]. The thermal spin polarization at $T = 1.55$ K and with the magnetic field on resonance is 1.9% [21]. With these values, we obtain for the CR a collective-coupling rate $g_{eff,inhom}/2\pi = 645.1$ kHz, overestimating the measured value by more than 40%. This deviation can be explained by a finite gap between the resonator and the Si:P crystal, reducing the effective filling factor.

To analyze the dependence of the effective coupling rate on the finite gap size d_{gap}, we calculate the filling factor R_{yz} for the different designs by taking only B_1^{yz} for $z \geq d_{gap}$ in Eq. (6) into account. We plot R_{yz} as a function of d_{gap} in Fig. 6(b). We observe a qualitative difference between the CR and/or MR and the SR. Due to the short decay length of the dynamic magnetic field for the CR and MR, a finite gap results in a significant effect on the coupling strength for these two designs. In contrast, the larger mode volume of the SR leads to a more favorable dependence. Due to the different ratio of components of the dynamic magnetic field perpendicular to the static magnetic field, the maximum value for d_{gap} differs for the three designs. We find a maximum value of $R_{yz,SR} = 0.440$ for the spiral resonator, $R_{yz,CR} = 0.481$ for the CR and $R_{yz,MR} = 0.491$ for the MR.

Using the data presented in Fig. 6(b), we can estimate the nominal gap between the Si:P crystal and the resonator plane. The measured collective-coupling rate of 384.8 kHz corresponds to a gap of $d_{gap,CR} = 3.80 \pm 0.09$ μm. We perform the same analysis of the collective coupling for the SR and MR and present the extracted parameters in Table I.

From our simulations, we are able to estimate the number of spins addressed in the measurement using the 3D field distribution and the collective-coupling rate from experiment and obtain $N = 4.16 \times 10^9$. A comparison of this number to the number of excitations in the resonator using Eq. (7), $n_{ph} = 7800$, confirms that we are in the low-excitation regime. Since $N \gg n_{ph}$, our modeling of the collective coupling is valid, even though the resonator is not in the ground state [22]. It is therefore also applicable at millikelvin temperatures in the context of ultrasensitive solid-state ESR.

E. Power saturation

Our theoretical model also allows us to calculate the collective-coupling strength as a function of the applied microwave power and to take the effects of power saturation into account. In electron spin resonance, power saturation is a well-known phenomenon [54,55], which leads to a modulation of the ESR signal as a function of the applied microwave power. As the power level increases, the spin system is driven into saturation. This also has an effect on the collective-coupling rate g_{eff}, as it leads to an effective decoupling of the spin system from the microwave resonator [56].

In Fig. 7, we plot the collective-coupling rate as a function of the applied power for the three resonator geometries. The collective-coupling rates are obtained using the procedure described in the previous section. The SR and MR achieve the highest coupling rates, of about 450 kHz. All three curves show a decrease of the collective coupling with increasing power, suggesting a power-dependent saturation effect.

In order to model the power dependence, we take the saturation of the ESR signal into account. In a continuous-wave ESR experiment, the signal increases with the microwave driving field B_1 and the signal intensity is therefore given by the following [57]:

$$S = \frac{S_0 B_1}{(1 + s\gamma^2 B_1^2 T_1 T_2)^{1/2}}. \quad (11)$$

Here, γ is the gyromagnetic ratio and T_1 and T_2 are the spin life time and spin coherence time, respectively. The exponent of $1/2$ is valid for an inhomogeneously broadened spin ensemble, which is the case for ^{nat}Si with abundant
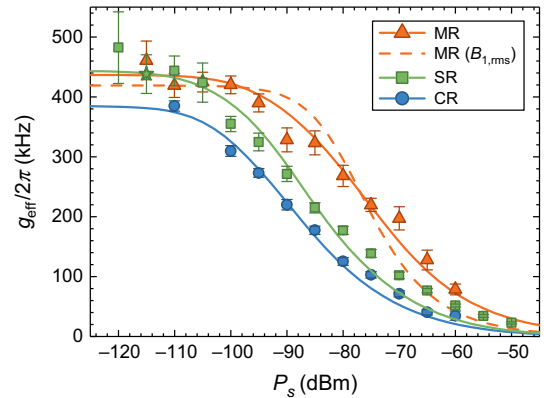

FIG. 7. The collective-coupling rate g_{eff} as a function of the power applied to the sample P_S. The collective-coupling rate g_{eff} decreases with increasing microwave power, indicating a power-dependent saturation effect. The solid lines are fits to Eq. (12), taking the simulated magnetic field distribution into account. The dashed line is a calculation using the root-mean-square (rms) field amplitude $B_{1,rms}$ of the CR.

[29]Si nuclei [51]. S_0 is a factor independent of B_1 and the factor $S_{\text{sat}} = 1/(1 + \gamma^2 B_1^2 T_1 T_2)^{1/2}$ models the power saturation. For $\gamma^2 B_1^2 \ll 1/(T_1 T_2)$, the denominator in Eq. (11) is equal to one and the spin ensemble is in the unsaturated regime. The correction factor s accounts for Lorentzian or Gaussian line shapes and is determined via a least-squares fitting procedure. For the B_1 field in this equation, we use the exported field distribution from our simulation data. We rescale the magnetic field in Eq. (11) according to $B_1 \propto \sqrt{P_S}$ to obtain a power-dependent expression. Using this result, we can modify Eq. (6) to take power saturation into account and obtain the following:

$$R_{yz,\text{sat}} = \frac{\sum_V |S_{\text{sat}}[B_{1,\text{sim}}^{yz}(\vec{r})] \cdot B_{1,\text{sim}}^{yz}(\vec{r})|^2}{\sum_{V_m} |B_{1,\text{sim}}^{xyz}(\vec{r})|^2}. \quad (12)$$

The solid lines in Fig. 7 are fits of Eq. (12) to the data, with the correction factor s being the only free parameter. The values of $T_1 = 48$ ms and $T_2 = 400$ ns are extracted from pulsed-ESR measurements. We obtain good agreement between the data and our model if the full field distribution is taken into account. If we use only the root-mean-square amplitude of the field distribution, we obtain significantly worse agreement between theory and experiment (dashed line). The good agreement of our model regarding the power saturation behavior again confirms our understanding of the spatial extent of the microwave excitation field.

V. DISCUSSION AND CONCLUSION

In this work, we present three different resonator designs. All of the designs offer distinct advantages and therefore choosing the appropriate resonator geometry depends on the intended application. Superconducting planar resonators are used in two different experimental configurations with a different interface between the spin ensemble and the microwave resonator. First, one widely used method is the flip-chip configuration, in which the spin sample is placed on top of the resonator while the resonator itself is placed onto a separate substrate (see, e.g., Refs. [17,19–21] and this work). This type of sample mounting offers greater experimental flexibility, as the sample preparation and placement is independent of the fabrication of the resonator. However, due to the flip-chip geometry, the presence of a small gap between the microwave resonator and the spin sample is highly likely, in particular when working with solid-state samples. Another option is to pattern the microwave resonator directly onto a substrate that already contains the spin ensemble (see, e.g., Refs. [14,15,58]). Here, the direct interface between the spin ensemble and the microwave resonator offers the largest spin-photon coupling rates but comes with the disadvantage of strain-induced spin-resonance shifts [59]. The latter, for example, are caused by the different lattice constants and thermal expansion coefficients of the substrate and the superconducting thin-film material of the resonator.

From our simulation and experimental results, we can draw two conclusions. First, the simulated field distribution of the SR shows that this design is favorable for a homogeneous excitation of the spin ensemble in a flip-chip geometry. The microwave magnetic field decays slowly along the z direction and therefore offers spin excitation throughout the whole spin-sample region, even for bulk samples. This makes this design more robust against the presence of a gap between the resonator and the spin sample. For a better controlled resonator-to-spin sample distance and an even more enhanced field homogeneity, a thin polyimid (Kapton) spacer can be inserted between the microwave resonator and the spin sample to avoid B_1 inhomogeneities in the near field of the resonator [7]. From the simulations of the SR, we find an extended region of 20 μm thickness with a homogeneity better than 10%, comparable to that of commercial microwave resonators.

Second, if high single-spin coupling rates are desired, a resonator with a meander-shaped strip patterned directly on top of a thin layer containing the spin ensemble offers the best performance. In particular, the CR design with its large finger capacitor and therefore small inductance offers a high current density and therefore a large B_1 field, increasing the single-spin coupling rate [58]. Additionally, the periodic pattern of the meandering wire allows one to engineer microwave antennas that emit microwaves with a specific wave vector. This is a concept that is widely used in spin-wave-resonance spectroscopy, where excitation at a nonzero wave vector is desirable [60].

To summarize, we analyze three designs for superconducting planar lumped-element resonators. We perform FEM simulations to extract the resonance frequency and the quality factor as well as to calculate the characteristic magnetic field distribution of each resonator. We obtain good agreement between the simulations and the experimental results of fabricated chips, where the resonators are structured into a 150-nm Nb film. The spiral resonator exploits the 2D coil-like arrangement of the resonator wire to obtain an improved magnetic field homogeneity as well as an increased filling factor when a finite gap between the Si:P crystal and resonator is present. To demonstrate the feasibility of the resonators for magnetic resonance experiments, we present continuous-wave ESR measurements on phosphorus-doped [nat]Si using all three resonator designs. In order to explain the extracted collective-coupling rates, we extend our existing theoretical model to take the simulated microwave magnetic field distribution into account and find good agreement between the data and the model. Finally, we extract the collective-coupling rate as a function of the applied microwave power and simulate the saturation behavior using our model. Our

research demonstrates the feasibility of FEM simulations to extract the expected collective-coupling rate of a spin ensemble coupled to a microwave resonator and gives insight into the different application cases of the resonator designs.

APPENDIX: COLLECTIVE COUPLING IN AN INHOMOGENEOUS MAGNETIC FIELD

In the following, we derive an expression allowing us to calculate the collective-coupling rate g_{eff} for a spatially inhomogeneous distribution of the dynamic magnetic field. We start with the case of a homogeneous field.

The collective-coupling strength of a spin ensemble of N spins is given by Ref. [13] as $g_{\mathrm{eff}} = \sqrt{\sum_j^N |g_j|^2}$, where g_j is the single-spin coupling strength of an individual spin in the ensemble. In the case of homogeneous coupling, this expression reduces to $g_{\mathrm{eff}} = g_0 \sqrt{N}$ with the single-spin coupling rate given by the following [10]:

$$g_0 = \frac{g_s \mu_B}{2\hbar} B_{1,0}. \tag{A1}$$

Here, the coupling strength is determined by the magnetic component of the microwave vacuum field, $B_{1,0}$. This field can be estimated by integrating the energy stored in the magnetic field created by vacuum fluctuations, according to Ref. [36]:

$$\frac{\hbar \omega_r}{4} = \frac{1}{2\mu_0} \int_{V_m} B_1^2 \, dV = \frac{B_{1,0}^2 V_m}{2\mu_0}. \tag{A2}$$

The additional factor of 2 in the denominator on the left-hand side of the equation takes into account the fact that half of the energy is stored in the electric component of the vacuum field. Using Eqs. (A1) and (A2), the collective-coupling strength for a spatially homogeneous field distribution is given by the following:

$$g_{\mathrm{eff,hom}} = \frac{g_s \mu_B}{2\hbar} \sqrt{\frac{\mu_0 \rho_{\mathrm{eff}} \hbar \omega_r \nu}{2}}, \tag{A3}$$

where we have substituted $N = \rho_{\mathrm{eff}} V$ with the effective spin density ρ_{eff} and the spin sample volume V. The ratio $\nu = V/V_m$ is called the filling factor and defines the volume of the resonator field filled with the spin ensemble.

In the case of planar resonators, the assumption of a spatially homogeneous B_1 field is not valid. Here, we have

to take into account the spatial dependence of $B_1(\vec{r})$ in Eq. (A2). Another point to consider is the orientation of the B_1 field with respect to the static magnetic field $\vec{B}_0$. In our experiments, the static field is applied in plane along the x axis (cf. Fig. 1). Only field components B_1^{yz} perpendicular to $\vec{B}_0$ can excite spins in the spin ensemble. From our simulations, we export the 3D magnetic field $B_{1,\mathrm{sim}}(\vec{r})$, discretized into finite elements with volume $\Delta V = \Delta x \Delta y \Delta z$. Assuming that the field is homogeneous over the spatial extent of a single volume element, for the collective-coupling strength of a single volume element, we find the following:

$$\tilde{g}_{\mathrm{eff}}(\vec{r}) = \frac{g_s \mu_B}{2\hbar} \left[\alpha B_{1,\mathrm{sim}}^{yz}(\vec{r}) \right] \sqrt{\rho_{\mathrm{eff}} \Delta V}, \tag{A4}$$

where $B_{1,\mathrm{sim}}^{yz}(\vec{r})$ is the exported field amplitude of the volume element and $\rho_{\mathrm{eff}} \Delta V$ is the number of spins in the volume element. The calibration factor α rescales the field amplitude from the simulated excitation level to the level of vacuum fluctuations. It can be calculated similarly to Eq. (A2), as follows:

$$\frac{\hbar \omega_r}{4} = \frac{1}{2\mu_0} \int_{V_m} \left[\alpha B_{1,\mathrm{sim}}^{xyz}(\vec{r}) \right]^2 \, dV. \tag{A5}$$

Note that here we also take the x component of the B_1 field into account. We convert the integration into a summation over all volume elements and find, for the calibration factor,

$$\alpha = \sqrt{\frac{\mu_0 \hbar \omega_r}{2\Delta V \sum_{\Delta V} \left[B_{1,\mathrm{sim}}^{xyz}(\vec{r}) \right]^2}}. \tag{A6}$$

Combining Eqs. (A4) and (A6) and summing over all volume elements, we finally obtain an expression for the collective-coupling strength of a spin ensemble coupled to an inhomogeneous microwave magnetic field:

$$\begin{aligned} g_{\mathrm{eff}} &= \sqrt{\sum_{\Delta V} |\tilde{g}_{\mathrm{eff}}|^2} \\ &= \frac{g_s \mu_B}{2\hbar} \sqrt{\frac{\mu_0 \hbar \omega_r \rho_{\mathrm{eff}}}{2}} \sqrt{\frac{\sum_{\Delta V} |B_{1,\mathrm{sim}}^{yz}(\vec{r})|^2}{\sum_{\Delta V} |B_{1,\mathrm{sim}}^{xyz}(\vec{r})|^2}}. \end{aligned} \tag{A7}$$

Note that in this expression the size of the volume element ΔV effectively cancels out. The last square-root term plays a similar role to the filling factor ν introduced in Eq. (A3).

[1] Charles P. Poole, *Electron Spin Resonance: A Comprehensive Treatise on Experimental Techniques* (Dover Publications, Mineola, NY, 1996).

[2] Arthur Schweiger and Gunnar Jeschke, *Principles of Pulse Electron Paramagnetic Resonance* (Oxford University Press, Oxford, UK, 2001).

[3] R. Narkowicz, D. Suter, and R. Stonies, Planar microresonators for EPR experiments, J. Magn. Reson. **175**, 275 (2005).

[4] R. Narkowicz, D. Suter, and I. Niemeyer, Scaling of sensitivity and efficiency in planar microresonators for electron spin resonance, Rev. Sci. Instrum. **79**, 084702 (2008).

[5] A. C. Torrezan, T. P. Mayer Alegre, and G. Medeiros-Ribeiro, Microstrip resonators for electron paramagnetic resonance experiments, Rev. Sci. Instrum. **80**, 075111 (2009).

[6] H. Malissa, D. I. Schuster, A. M. Tyryshkin, A. A. Houck, and S. A. Lyon, Superconducting coplanar waveguide resonators for low temperature pulsed electron spin resonance spectroscopy, Rev. Sci. Instrum. **84**, 025116 (2013).

[7] O. W. B. Benningshof, H. R. Mohebbi, I. A. J. Taminiau, G. X. Miao, and D. G. Cory, Superconducting microstrip resonator for pulsed ESR of thin films, J. Magn. Reson. **230**, 84 (2013).

[8] A. J. Sigillito, H. Malissa, A. M. Tyryshkin, H. Riemann, N. V. Abrosimov, P. Becker, H.-J. Pohl, M. L. W. Thewalt, K. M. Itoh, J. J. L. Morton, A. A. Houck, D. I. Schuster, and S. A. Lyon, Fast, low-power manipulation of spin ensembles in superconducting microresonators, Appl. Phys. Lett. **104**, 222407 (2014).

[9] M. H. Devoret and R. J. Schoelkopf, Superconducting circuits for quantum information: An outlook, Science **339**, 1169 (2013).

[10] J. H. Wesenberg, A. Ardavan, G. A. D. Briggs, J. J. L. Morton, R. J. Schoelkopf, D. I. Schuster, and K. Mølmer, Quantum Computing with an Electron Spin Ensemble, Phys. Rev. Lett. **103**, 070502 (2009).

[11] H. Wu, R. E. George, J. H. Wesenberg, Klaus Mølmer, D. I. Schuster, R. J. Schoelkopf, K. M. Itoh, A. Ardavan, J. J. L. Morton, and G. A. D. Briggs, Storage of Multiple Coherent Microwave Excitations in an Electron Spin Ensemble, Phys. Rev. Lett. **105**, 140503 (2010).

[12] Eisuke Abe, Hua Wu, Arzhang Ardavan, and John J. L. Morton, Electron spin ensemble strongly coupled to a three-dimensional microwave cavity, Appl. Phys. Lett. **98**, 251108 (2011).

[13] K. Sandner, H. Ritsch, R. Amsüss, Ch. Koller, T. Nöbauer, S. Putz, J. Schmiedmayer, and J. Majer, Strong magnetic coupling of an inhomogeneous nitrogen-vacancy ensemble to a cavity, Phys. Rev. A **85**, 053806 (2012).

[14] S. Probst, A. Bienfait, P. Campagne-Ibarcq, J. J. Pla, B. Albanese, J. F. Da Silva Barbosa, T. Schenkel, D. Vion, D. Esteve, K. Mølmer, J. J. L. Morton, R. Heeres, and P. Bertet, Inductive-detection electron-spin resonance spectroscopy with 65 spins/Hz sensitivity, Appl. Phys. Lett. **111**, 202604 (2017).

[15] A. Bienfait, J. J. Pla, Y. Kubo, M. Stern, X. Zhou, C. C. Lo, C. D. Weis, T. Schenkel, M. L. W. Thewalt, D. Vion, D. Esteve, B. Julsgaard, K. Mølmer, J. J. L. Morton, and P. Bertet, Reaching the quantum limit of sensitivity in electron spin resonance, Nat. Nanotechnol. **11**, 253 (2016).

[16] A. Bienfait, P. Campagne-Ibarcq, A. H. Kiilerich, X. Zhou, S. Probst, J. J. Pla, T. Schenkel, D. Vion, D. Esteve,

J. J. L. Morton, K. Moelmer, and P. Bertet, Magnetic Resonance with Squeezed Microwaves, Phys. Rev. X **7**, 041011 (2017).

[17] Y. Kubo, F. R. Ong, P. Bertet, D. Vion, V. Jacques, D. Zheng, A. Dréau, J.-F. Roch, A. Auffeves, F. Jelezko, J. Wrachtrup, M. F. Barthe, P. Bergonzo, and D. Esteve, Strong Coupling of a Spin Ensemble to a Superconducting Resonator, Phys. Rev. Lett. **105**, 140502 (2010).

[18] D. I. Schuster, A. P. Sears, E. Ginossar, L. DiCarlo, L. Frunzio, J. J. L. Morton, H. Wu, G. A. D. Briggs, B. B. Buckley, D. D. Awschalom, and R. J. Schoelkopf, High-Cooperativity Coupling of Electron-Spin Ensembles to Superconducting Cavities, Phys. Rev. Lett. **105**, 140501 (2010).

[19] R. Amsüss, Ch. Koller, T. Nöbauer, S. Putz, S. Rotter, K. Sandner, S. Schneider, M. Schramböck, G. Steinhauser, H. Ritsch, J. Schmiedmayer, and J. Majer, Cavity QED with Magnetically Coupled Collective Spin States, Phys. Rev. Lett. **107**, 060502 (2011).

[20] S. Probst, H. Rotzinger, S. Wünsch, P. Jung, M. Jerger, M. Siegel, A. V. Ustinov, and P. A. Bushev, Anisotropic Rare-Earth Spin Ensemble Strongly Coupled to a Superconducting Resonator, Phys. Rev. Lett. **110**, 157001 (2013).

[21] Christoph W. Zollitsch, Kai Mueller, David P. Franke, Sebastian T. B. Goennenwein, Martin S. Brandt, Rudolf Gross, and Hans Huebl, High cooperativity coupling between a phosphorus donor spin ensemble and a superconducting microwave resonator, Appl. Phys. Lett. **107**, 142105 (2015).

[22] I. Chiorescu, N. Groll, S. Bertaina, T. Mori, and S. Miyashita, Magnetic strong coupling in a spin-photon system and transition to classical regime, Phys. Rev. B **82**, 024413 (2010).

[23] C. P. Wen, Coplanar waveguide: A surface strip transmission line suitable for nonreciprocal gyromagnetic device applications, IEEE Trans. Microw. Theory Tech. **17**, 1087 (1969).

[24] T. Lindström, J. E. Healey, M. S. Colclough, C. M. Muirhead, and A. Ya. Tzalenchuk, Properties of superconducting planar resonators at millikelvin temperatures, Phys. Rev. B **80**, 132501 (2009).

[25] Moe S. Khalil, F. C. Wellstood, and Kevin D. Osborn, Loss dependence on geometry and applied power in superconducting coplanar resonators, IEEE Trans. Appl. Supercond. **21**, 879 (2011).

[26] K. Geerlings, S. Shankar, E. Edwards, L. Frunzio, R. J. Schoelkopf, and M. H. Devoret, Improving the quality factor of microwave compact resonators by optimizing their geometrical parameters, Appl. Phys. Lett. **100**, 192601 (2012).

[27] W. J. Wallace and R. H. Silsbee, Microstrip resonators for electron-spin resonance, Rev. Sci. Instrum. **62**, 1754 (1991).

[28] E. Kupce and R. Freeman, Adiabatic pulses for wideband inversion and broadband decoupling, J. Magn. Reson., Ser. A **115**, 273 (1995).

[29] Alberto Tannús and Michael Garwood, Adiabatic pulses, NMR Biomed. **10**, 423 (1997).

[30] Michael Garwood and Lance DelaBarre, The return of the frequency sweep: Designing adiabatic pulses for contemporary NMR, J. Magn. Reson. **153**, 155 (2001).

[31] Thomas E. Skinner, Michael Braun, Klaus Woelk, Naum I. Gershenzon, and Steffen J. Glaser, Design and application of robust rf pulses for toroid cavity NMR spectroscopy, J. Magn. Reson. **209,** 282 (2011).

[32] Philipp E. Spindler, Yun Zhang, Burkhard Endeward, Naum Gershernzon, Thomas E. Skinner, Steffen J. Glaser, and Thomas F. Prisner, Shaped optimal control pulses for increased excitation bandwidth in EPR, J. Magn. Reson. **218,** 49 (2012).

[33] J. P. Turneaure, J. Halbritter, and H. A. Schwettman, The surface impedance of superconductors and normal conductors: The Mattis-Bardeen theory, J. Supercond. **4,** 341 (1991).

[34] M. Göppl, A. Fragner, M. Baur, R. Bianchetti, S. Filipp, J. M. Fink, P. J. Leek, G. Puebla, L. Steffen, and A. Wallraff, Coplanar waveguide resonators for circuit quantum electrodynamics, J. Appl. Phys. **104,** 113904 (2008).

[35] A. Megrant, C. Neill, R. Barends, B. Chiaro, Y. Chen, L. Feigl, J. Kelly, Erik Lucero, Matteo Mariantoni, P. J. J. O'Malley, D. Sank, A. Vainsencher, J. Wenner, T. C. White, Yu Yin, J. Zhao, C. J. Palmstrøm, John M. Martinis, and A. N. Cleland, Planar superconducting resonators with internal quality factors above one million, Appl. Phys. Lett. **100,** 113510 (2012).

[36] R. J. Schoelkopf and S. M. Girvin, Wiring up quantum systems, Nature **451,** 664 (2008).

[37] Alexandre Blais, Ren-Shou Huang, Andreas Wallraff, S. M. Girvin, and R. J. Schoelkopf, Cavity quantum electrodynamics for superconducting electrical circuits: An architecture for quantum computation, Phys. Rev. A **69,** 062320 (2004).

[38] Cècile Grézes, Towards a Spin Ensemble Quantum Memory for Superconducting Qubits, Ph.D. thesis, CEA Saclay (2015).

[39] Guilherme Tosi, Fahd A. Mohiyaddin, Hans Huebl, and Andrea Morello, Circuit-quantum electrodynamics with direct magnetic coupling to single-atom spin qubits in isotopically enriched ^{28}Si, AIP Adv. **4,** 087122 (2014).

[40] R. H. Dicke, Coherence in spontaneous radiation processes, Phys. Rev. **93,** 99 (1954).

[41] Hans Huebl, Christoph W. Zollitsch, Johannes Lotze, Fredrik Hocke, Moritz Greifenstein, Achim Marx, Rudolf Gross, and Sebastian T. B. Goennenwein, High Cooperativity in Coupled Microwave Resonator Ferrimagnetic Insulator Hybrids, Phys. Rev. Lett. **111,** 127003 (2013).

[42] CST Computer Simulation Technology GmbH, CST MICROWAVE STUDIO 2016 (2016).

[43] D. C. Mattis and J. Bardeen, Theory of the anomalous skin effect in normal and superconducting metals, Phys. Rev. **111,** 412 (1958).

[44] T. Niemczyk, F. Deppe, M. Mariantoni, E. P. Menzel, E. Hoffmann, G. Wild, L. Eggenstein, A. Marx, and R. Gross, Fabrication technology of and symmetry breaking in superconducting quantum circuits, Supercond. Sci. Technol. **22,** 034009 (2009).

[45] S. Probst, F. B. Song, P. A. Bushev, A. V. Ustinov, and M. Weides, Efficient and robust analysis of complex scattering data under noise in microwave resonators, Rev. Sci. Instrum. **86,** 024706 (2015).

[46] Edward H. Poindexter, Philip J. Caplan, Bruce E. Deal, and Reda R. Razouk, Interface states and electron spin resonance centers in thermally oxidized (111)

and (100) silicon wafers, J. Appl. Phys. **52,** 879 (1981).

[47] A. Stesmans and V. V. Afanas'ev, Electron spin resonance features of interface defects in thermal (100)Si/SiO$_2$, J. Appl. Phys. **83,** 2449 (1998).

[48] G. Feher, R. C. Fletcher, and E. A. Gere, Exchange effects in spin resonance of impurity atoms in silicon, Phys. Rev. **100,** 1784 (1955).

[49] D. Jérome and J. M. Winter, Electron spin resonance on interacting donors in silicon, Phys. Rev. **134,** A1001 (1964).

[50] Peter F. Herskind, Magnus Albert, and Michael Drewsen, Realization of collective strong coupling with ion Coulomb crystals in an optical cavity, Nat. Phys. **5,** 494 (2009).

[51] Eisuke Abe, Alexei M. Tyryshkin, Shinichi Tojo, John J. L. Morton, Wayne M. Witzel, Akira Fujimoto, Joel W. Ager, Eugene E. Haller, Junichi Isoya, Stephen A. Lyon, Mike L. W. Thewalt, and Kohei M. Itoh, Electron spin coherence of phosphorus donors in silicon: Effect of environmental nuclei, Phys. Rev. B **82,** 121201 (2010).

[52] We estimate the contribution to the inhomogeneous broadening due to an inhomogeneous B_0 field to be less than 17 μT, based on the specified field homogeneity of the solenoid. Due to the way in which the Si:P crystal is mounted on the resonator, the influence of strain on the inhomogeneous broadening is negligible.

[53] In our calculation, we use the nominal donor concentration ρ as the density, assuming that each donor contributes equally to the collective coupling. However, for donor concentrations $N_D \gtrsim 5 \times 10^{16}$ cm^{-3}, phosphorus dimers and trimers are formed, which also contribute to the broad background signal and the P$_2$ dimer transition. We therefore calculate the theoretical upper bound of the collective coupling.

[54] T. G. Castner, Saturation of the paramagnetic resonance of a V center, Phys. Rev. **115,** 1506 (1959).

[55] P. R. Cullis, Electron paramagnetic resonance in inhomogeneously broadened systems: A spin temperature approach, J. Magn. Reson. (1969) **21,** 397 (1976).

[56] Andreas Angerer, Stefan Putz, Dmitry O. Krimer, Thomas Astner, Matthias Zens, Ralph Glattauer, Kirill Streltsov, William J. Munro, Kae Nemoto, Stefan Rotter, Jörg Schmiedmayer, and Johannes Majer, Ultralong relaxation times in bistable hybrid quantum systems, Sci. Adv. **3,** e1701626 (2017).

[57] P. Fajer, A. Watts, and D. Marsh, Saturation transfer, continuous wave saturation, and saturation recovery electron spin resonance studies of chain-spin labeled phosphatidylcholines in the low temperature phases of dipalmitoyl phosphatidylcholine bilayers. Effects of rotational dynamics and spin-spin interactions, Biophys. J. **61,** 879 (1992).

[58] C. Eichler, A. J. Sigillito, S. A. Lyon, and J. R. Petta, Electron Spin Resonance at the Level of 10^4 Spins Using Low Impedance Superconducting Resonators, Phys. Rev. Lett. **118,** 037701 (2017).

[59] J. J. Pla, A. Bienfait, G. Pica, J. Mansir, F. A. Mohiyaddin, Z. Zeng, Y. M. Niquet, A. Morello, T. Schenkel, J. J. L. Morton, and P. Bertet, Strain-Induced Spin-Resonance Shifts in Silicon Devices, Phys. Rev. Appl. **9,** 044014 (2018).

[60] Matthieu Bailleul, Dominik Olligs, and Claude Fermon, Propagating spin wave spectroscopy in a permalloy film: A quantitative analysis, Appl. Phys. Lett. **83,** 972 (2003).